*Solar RRL*

WILEY-VCH

RESEARCH ARTICLE OPEN ACCESS

# Advanced Solar Cells with Thermal, Radiation, and Light Management for Space-Based Solar Power

Eduardo Camarillo Abad[1] | Kai Sun[2] | Armin Barthel[1,3] | Oliver Trojak[2] | Nikolaos Kalfagiannis[4,5] | Demosthenes C. Koutsogeorgis[5] | Nina Vaidya[2] | Otto L. Muskens[2] | Louise C. Hirst[1,3]

[1]Department of Physics, University of Cambridge, Cambridge, UK | [2]Faculty of Engineering and Physical Sciences, University of Southampton, Southampton, UK | [3]Department of Materials Science and Metallurgy, University of Cambridge, Cambridge, UK | [4]Department of Materials Science and Engineering, University of Ioannina, Ioannina, Greece | [5]School of Science and Technology, Nottingham Trent University, Nottingham, UK

**Correspondence:** Eduardo Camarillo Abad (ec675@cam.ac.uk) | Nina Vaidya (n.vaidya@soton.ac.uk) | Otto L. Muskens (o.muskens@soton.ac.uk) | Louise C. Hirst (lh619@cam.ac.uk)

**Received:** 8 February 2025 | **Revised:** 10 March 2025 | **Accepted:** 11 March 2025

**Funding:** UK Department for Energy Security and Net Zero, Grant/Award Number: SBSP1003; H2020 European Research Council, Grant/Award Number: Grant/Award Number: 853365

**Keywords:** concentrator photovoltaics | passive radiative cooling | photovoltaics | space-based solar power | ultra-thin photovoltaics

## ABSTRACT

Space-based solar power (SBSP) can provide clean and continuous baseload energy by beaming solar power to our planet from photovoltaic arrays in space. While it is widely acknowledged that gigawatt-level, kilometer-scale solar stations in space are required to make SBSP a cost-competitive energy source, these systems can only be viable by implementing lightweight, radiation tolerant, deployable, and low-cost photovoltaic technologies. Here, advanced solar cells with thermal, radiation, and light management (ASTRAL) is presented, a photovoltaic device conceived for SBSP that consists of an ultra-thin tandem solar cell with flexible form factors, ultra-low weight, intrinsic radiation tolerance, and integrated light and thermal management. Through rigorous thermal, radiation, and optical device modeling, it is demonstarted that ASTRAL achieves decades-long lifetimes on SBSP-relevant orbits with $>30\times$ reduction in radiation shielding mass and corresponding launch costs, all while enabling power generation in excess of 1 kW/m$^2$ at operating temperatures <100°C. Together, these properties make ASTRAL a state-of-the-art photovoltaic technology and a compelling candidate for the practical delivery of SBSP.

## 1 | Introduction

Space-based solar power (SBSP) foresees the collection of solar power in space by photovoltaic arrays, the transmission of the collected power to Earth via microwaves, and the conversion of the received energy to electricity that can be fed into the grid or used in remote locations [1, 2]. This visionary technology could deliver near-continuous and low-carbon power to ground-based receivers, unhindered by diurnal, annual, or meteorological changes.

While it is widely acknowledged that GW-level installations are needed for SBSP to be a cost-competitive energy source, generating this power would require the manufacture, launch, and in-space assembly of km-scale solar power stations. Further intrinsic challenges include the minimization of losses throughout the various energy conversion steps and the need for large ground receiving areas due to the diffraction of the transmitted beam from orbit. However, despite its ambitious nature, the urgency of climate change mitigation and the recent fall in launch costs are fueling increased efforts to deliver SBSP within the coming decades. Worldwide advancements span from research and development agendas to feasibility studies [3], proposals for SBSP station architectures [4–6], developments in power collection and wireless transmission technologies [7, 8], and prototype testing both in terrestrial and space environments [9].

Amongst the necessary advancements for SBSP, developments on the photovoltaic (PV) components are crucial for the success of this technology. First, cells must have high radiation tolerance and survive for decades in high-altitude orbits. These space environments enable continuous ground coverage and uninterrupted power transmission for SBSP stations [10], but have high fluxes of damaging particles (e.g., electrons and protons) that progressively degrade device performance by introducing defects in the cells. Next, implementing ultra-lightweight technologies with high specific power (power-to-mass ratio) is vital considering the enormous PV areas required for GW-scale SBSP. These large areas also call for PV technologies with low array cost, particularly as launch costs decrease making component expenses more significant. Finally, PV for SBSP would also benefit from a deployable design that facilitates the on-orbit assembly of the system.

Currently, no space PV design meets all the criteria to deliver SBSP. State-of-the-art III–V multi-junction solar cells at or above \$40/W would result in array costs on the order of billions of dollars to produce power on the GW-scale [11]. This pricepoint has led many SBSP whole system designs to consider the implementation of concentrator technologies, which employ small area cells, to reduce costs [7, 12]. However, as heat dissipation in space is restricted to radiative cooling, this strategy needs efficient thermal management to deliver sufficient power whilst avoiding prohibitive cell temperatures [10, 13]. Additionally, the current strategy to shield space solar cells from radiation damage and achieve long system lifetimes is to interface the PV with heavy coverglass layers. This approach limits the form factors of the device, and could be restrictive for SBSP where a km$^2$ station would imply the addition of hundreds of tonnes of radiation shielding mass, with a corresponding ∼\$100 M increase in launch costs [14].

Delivering the ambitious goals of SBSP requires equally disruptive PV technologies beyond present paradigms. Herein, we present ASTRAL (advanced solar cells with thermal, radiation, and light management), a next-generation PV technology conceived for SBSP. ASTRAL consists of a concentrator solar cell with i) intrinsic radiation tolerance, offering decades-long lifetimes in high-altitude, continuous-coverage orbits without heavy coverglass; ii) high specific power, reducing radiation shielding mass by one order of magnitude whilst delivering power in excess of 1 kW/m$^2$ to meet the demands of SBSP stations; iii) flexible and deployable form factors; and iv) state-of-the-art lightweight passive cooling, maintaining operating temperatures below 100°C under concentration. Together, these functionalities make ASTRAL a promising PV technology to provide economic delivery of energy from space. Beyond SBSP, ASTRAL is also a compelling technology for other space missions in hostile environments, where its radiation resilience is desirable, while its lightweight flexible form factors may be advantageous for other applications such as vehicle integration.

## 2 | Coupling Key Functionalities for SBSP in ASTRAL

ASTRAL has four main components (Figure 1a): an ultra-thin tandem solar cell, a rear light-trapping texture, a lightweight reflective substrate, and a multifunctional front coating (MFC). The synergy of these components enables long lifetimes in hostile space environments, high specific power, and regulated operating temperatures under concentration.

In this work, we propose a tandem solar cell with ultrathin (∼100 nm) GaAs and InGaP subcells. This highly reduced

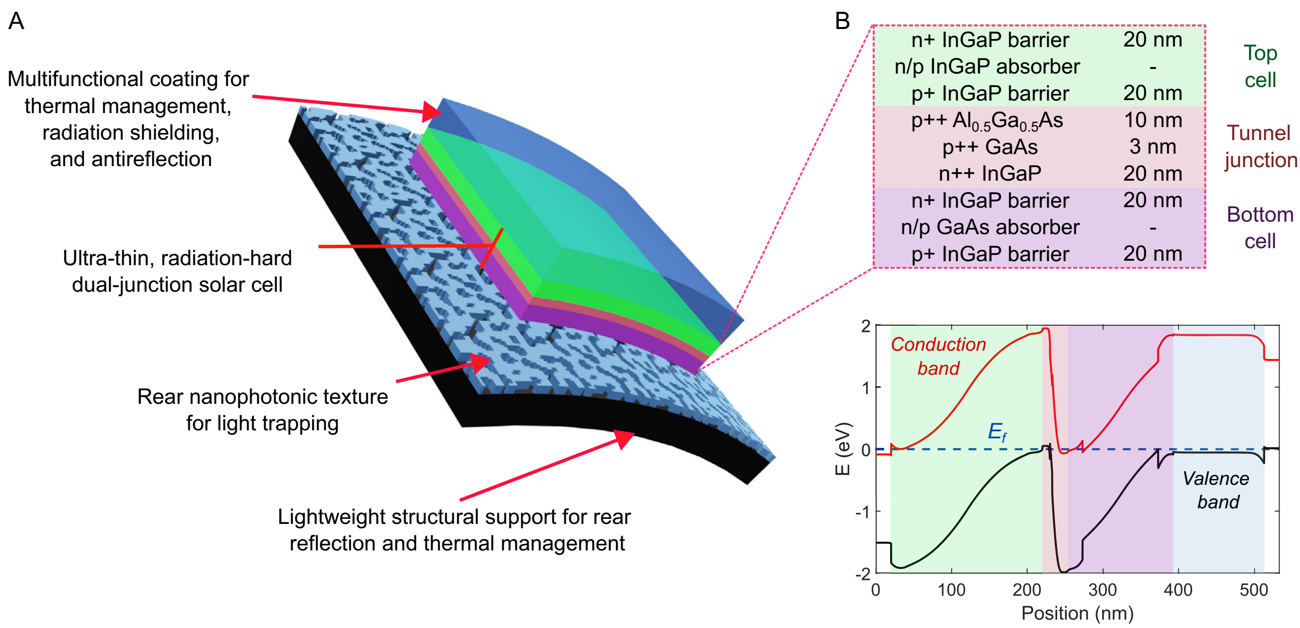


**FIGURE 1** | ASTRAL holds key functionalities for SBSP: high specific power, deployability, longevity in hostile space orbits, and regulated operating temperatures under concentration. These functionalities are unlocked by the synergy of four components (A): a multifunctional front coating, an ultrathin dual-junction solar cell, a rear nanophotonic texture, and a lightweight structural support. (B) In particular for the tandem cell, the proposed layer structure provides a favorable band structure, calculated with Poisson drift-diffusion simulations [15] for representative absorber thicknesses and assuming the addition of highly-doped GaAs contact layers. Device diagram is representative, not to scale, and does not show contacting schemes.

length-scale is critical to unlock device performance that is inherently resilient to radiation damage [16–18]. It also impacts on component cost, offering a significant reduction in growth reactor time compared to current industry standard III–V triple junction space PV and a corresponding increase in production volumes (~50% higher). For the purpose of the simulations presented in this work a realistic full device layer structure is employed (Figure 1a). Both subcells employ highly doped InGaP barrier layers. These have demonstrated self-passivation properties in ultra-thin devices, which are fully depleted and therefore surface sensitive, with nearly all carriers generated in these passivation layers contributing to the photocurrent [19]. As such, InGaP barriers are preferred over other wide bandgap alloys (e.g., AlGaInP or InAlP) that are commonly implemented in thicker tandem designs [20–26]). On the contrary, the tunnel junction consists of a highly doped $Al_{0.5}Ga_{0.5}As$ (p++)/GaAs (p++)/InGaP (n++) structure, which has demonstrated high current densities suitable for concentrator applications [27–29] and holds improved transparency over other widely employed strategies such as AlGaAs (p++)/GaAs (n++) structures [20, 21, 23, 30]. A representative band structure for this tandem device is shown in Figure 1b, assuming charge transport through the texture and the addition of highly doped GaAs layers to create localised contacts (the back reflector and the MFC are not considered to be electrical device components).

The light-trapping texture in ASTRAL allows for efficient photon harvesting in the otherwise highly-transmissive ultra-thin subcells, by enabling coupling to waveguide resonances and total internal reflection of scattered waves within the cell. The strategy we study in this work consists of a nanophotonic scattering surface (Figure 1a) below the bottom cell, made of a high-band gap semiconductor and a low-index dielectric ($Al_{0.5}Ga_{0.5}As$ and $SiO_2$). The rear location of the texture aims to maximize its efficiency, as scattering layers made of material pairs with high index contrast are promising for light trapping [31], but these materials tend to have non-negligible absorption at short wavelengths which would be prohibitive for device performance if placed on the front surface. The texture design has a quasi-random geometry and high transparency, which has been shown to enable broadband absorption enhancement and rich modal structures in ultra-thin photovoltaics [32, 33], leading to state-of-the-art device performance in patterned cells [34]. It is envisaged that a low cost, large area patterning technique such as polymer blend lithography would be employed to fabricate these structures [34]. The epitaxial III–V device layer structure is removed from its growth wafer to form the optical cavity using techniques such as epitaxial lift-off [35–38] or spalling [39, 40]. Note that the quasi-random material arrangement is described by a square unit cell and has a periodicity that we refer to as the pitch.

The back reflector of ASTRAL (Figure 1a) minimizes transmission losses into the substrate, improves the optical cavity formed by the cell, and enables further absorption enhancement by means of Fabry Perot resonances. Here we consider a Ag mirror to be adjacent to the light-trapping texture, given the improved reflectance of this metal at visible wavelengths which benefits the photocurrent [41]. Note that this reflective surface is expected to be mounted on a lightweight and flexible substrate offering mechanical stability [42–44].

Finally, the multifunctional front coating (MFC) of ASTRAL acts as an antireflection coating at the operational wavelengths of the tandem cell, whilst also enabling IR emissivity for passive radiative cooling under concentration. In this work we consider a multilayered coating made of $SiO_2$, SiN, $Ta_2O_5$, and Al:ZnO (AZO), with specific designs following from a full device optimization. These materials have suitable transparency at visible wavelengths and allow IR emission bands at $\lambda \approx 2.5$–$25$ μm in line with space environment requirements (ESA standard ECSS-Q-ST-70-09C). The emissivity at the shorter end of this range ($\lambda \approx 2.5$–$7$ μm) is enabled by the AZO and is favorable for operation at elevated temperatures >100°C [45]. Note that the multifunctionality of the MFC goes beyond thermal and light management, as it also has radiation-shielding properties and protects the underlying tandem cell from low-energy particle damage. Additionally, we expect the MFC to offer sufficient protection from UV damage in the system.

The following sections present the operating principles of the components of ASTRAL, and demonstrate a design framework to holistically optimize these components to meet the PV requirements for SBSP. The particular concentration system employed with ASTRAL is not considered here, although we envision the integration of a reflective embodiment [42, 43].

## 3 | Coverglass-Free Longevity in Hostile Orbits

ASTRAL must survive prolonged exposure to the damaging radiation flux in space, which varies for different orbits in the near-Earth environment and primarily consists of energetic protons and electrons. Given that high altitude orbits with continuous ground coverage are coveted for SBSP, we focus on the Molniya and geostationary (GEO) orbits as representative radiation environments to study the longevity of ASTRAL. The energy distributions of radiation flux in these orbits are shown in Figure 2a,b for electrons and protons, respectively, together with data for the low Earth orbit of Phase 1 Starlink satellites for comparison. Also included is the variation of the non-ionizing energy loss (NIEL) with particle energy, which denotes the rate at which radiation incident on a target loses energy to atomic displacements [46], leading to the creation of defects. The data indicate that low-energy protons with high flux are expected to be most damaging to ASTRAL, whereas low energy electrons are not expected to cause any degradation (at least not by non-ionizing processes) despite their large flux in relevant orbits.

When exposed to these radiation environments, even a thin MFC can offer critical protection to ASTRAL by stopping low-energy particles and reducing the dose of radiation received by the device. This shielding mechanism is comparable to what is conventionally achieved with coverglass layers on space solar cells. The effectiveness of the MFC as a radiation shield can be estimated by calculating the maximum energies of particles that are completely stopped in 2 μm of each of its constituent dielectrics (see Section 8.2), which is comparable to the total thickness of the MFC designs in this work. The energy thresholds below which all protons stop in the MFC span from 252 keV for pure $SiO_2$ to 336 keV for pure $Al_2O_3$, with the other dielectrics lying within these limits (Figure 2b). In the context of our radiation

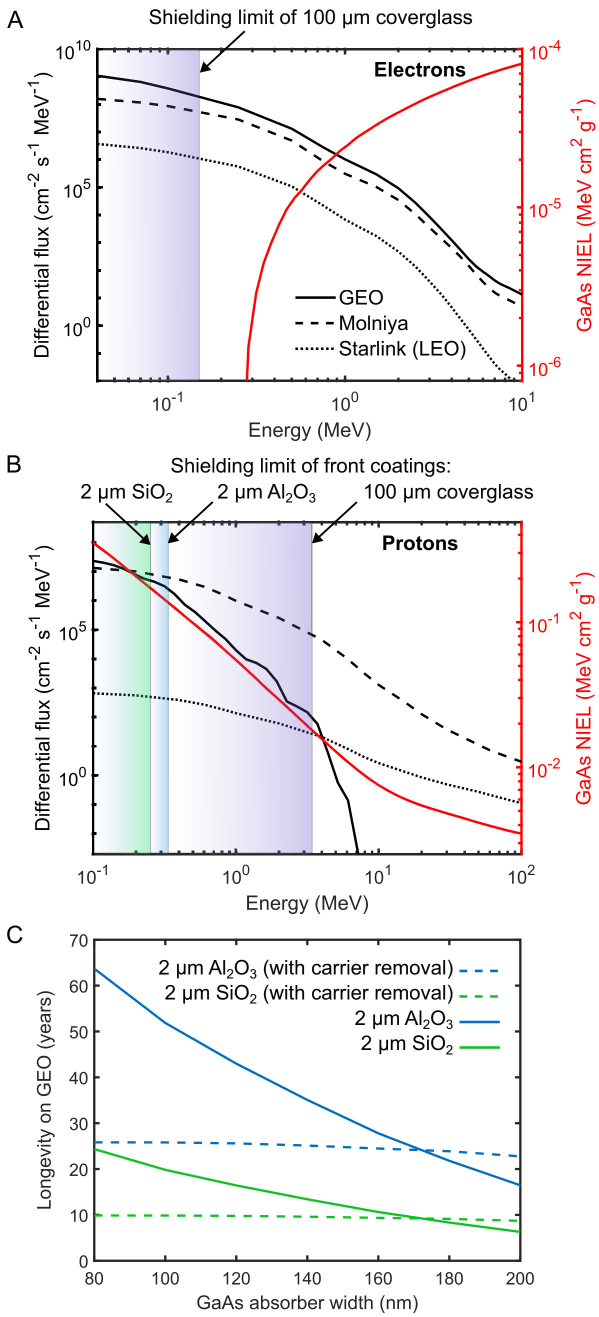


**FIGURE 2** | ASTRAL can survive for decades in the coveted space environments for SBSP without the need for heavy protective coverglass layers. SBSP-relevant orbits (Molniya and GEO) have high fluxes of energetic (A) protons and (B) electrons, particularly compared to a low Earth orbit (LEO). The rate at which these particles introduce defects in a GaAs cell is denoted by their non-ionizing energy loss (NIEL). In ASTRAL, the multifunctional front coating (MFC) would shield the underlying cell from a range of particle energies, as shown for 2 µm coatings of $SiO_2$ and $Al_2O_3$, which are representative of the minimum and maximum levels of shielding provided by the MFC. Given its intrinsic radiation tolerance, these levels of shielding are sufficient for the ultra-thin ASTRAL device to achieve lifetimes in the order of decades, as shown in (C) for a GEO orbit (longevity, or time to device failure, is modeled as the time when the carrier lifetime equals the transit time in the device, both considering and ignoring carrier removal effects). For comparison, standard space PV is an order of magnitude thicker, and achieves comparable lifetimes by integrating ~100 µm coverglass layers that represent >30× increase in shielding mass.

environments of interest, these thresholds indicate that the MFC can considerably decrease the maximum differential proton flux impinging on ASTRAL, an effect that is greatest in GEO where this reduction reaches 42% within the studied energy range (flux data is not available for proton energies <100 keV). As for electrons, the range of these particles in matter is generally greater than protons, and therefore even electrons with only 40 keV of kinetic energy (minimum available data [47]) are expected to pass through ~2 µm of the MFC dielectrics. Ultimately, while the MFC reduces the dose of harmful protons on ASTRAL, the device will still be exposed to damaging radiation fluxes during on-orbit operation. This exposure will be considerably higher than in conventional space solar cells, where much thicker (~100 µm) coverglass layers provide significantly larger radiation shielding to enable decades-long device lifetimes (see thresholds in Figure 2a,b).

To achieve longevity, ASTRAL trades the need for enhanced protection from increased front coating mass for an ultrathin (~100 nm) device structure that is intrinsically radiation resilient. On the ultrathin length-scale, the short travel distance required for carrier extraction enables efficient current collection, even in the presence of high-densities of radiation-induced defects. As a consequence, the photocurrent of ultra-thin devices does not degrade up to large radiation fluences, well beyond the degradation onset of conventional devices that are an order of magnitude thicker. More specifically, the $J_{sc}$ of ultra-thin devices has been shown to undergo a rapid collapse when radiation exposure reduces carrier lifetimes below the transit time in the device (i.e., the time that charge carriers need to cross the absorber layer) [17].

For the two-terminal tandem in ASTRAL, we expect that the collapse in the $J_{sc}$ will be dominated by the photocurrent degradation of the bottom cell, as InGaP is well-known to have significantly greater radiation tolerance than GaAs [48–50]. Therefore, taking the time for short-circuit current collapse as the point of device failure, the longevity of ASTRAL can be modeled by calculating the progressive degradation of carrier lifetime in the GaAs subcell for a given radiation environment (i.e., orbit), and finding the time where it becomes comparable to the transit time in the fully depleted ultra-thin subcell where carrier transport is dominated by drift. Herein, we model the variation of carrier lifetime with radiation exposure based on previous experimental studies [17] and calculate transit time from the drift-velocity equation (see Section 8.3 for more details). The latter calculations are performed both ignoring and accounting for carrier removal effects, where radiation-induced defects can affect the transit time by trapping majority carriers and reducing carrier concentrations, thereby varying the electric field that drives carrier drift in the device. We consider these two scenarios as carrier removal is known to affect conventional device performance [51–55], but its involvement in the short-circuit current collapse of ultra-thin solar cells has not yet been verified experimentally.

Based on this model, the longevity of ASTRAL as a function of the GaAs subcell thickness is calculated for GEO up to an absorber thickness of 200 nm (Figure 2c). Beyond this absorber thickness the applicability of the model breaks down due to the increased relevance of diffusion for carrier transport. Results are shown for the maximum (2 μm of $Al_2O_3$) and minimum (2 μm of $SiO_2$) extent of shielding from the MFC. Generally, the model shows that increments in absorber width come with longevity reductions, as the larger travel distance and lower electric field strength result in an increase in the transit time. Carrier removal effects reduce the variation with absorber width, given that the introduction of majority carrier traps eventually leads to doping compensation in the barrier layers. This phenomenon occurs at the same radiation dose regardless of the GaAs thickness, leading to a substantial drop in the electric field strength across the absorber layer and a large increase in transit time. More importantly, although carrier removal effects and the choice of MFC dielectric can have a significant effect on longevity, it is a remarkable finding that in all cases ASTRAL could survive for decades on a GEO orbit with only 2 μm of front surface protection, as opposed to the ~100 μm coverglass that is conventionally used to achieve lifetimes of this magnitude. This drastic difference entails >30× shielding mass reduction per PV unit area, representing launch cost savings in the order of \$100 M for the $km^2$ stations conceived for GW-scale SBSP.

## 4 | High Photon Harvesting in an Ultra-Thin Tandem Solar Cell

Maximizing the photocurrent is an important challenge for ASTRAL. As opposed to conventional thick tandems where the absorber layers have near-complete absorption of above-bandgap photons in a single-pass, our ultra-thin solar cell architecture is highly transmissive and requires the integration of an antireflection coating, rear mirror, and nanophotonic texture to enhance the $J_{sc}$ [56, 57]. These light-management platforms must be optimized to maximize absorption enhancement, all whilst ensuring that the corresponding field-enhancement mechanisms (e.g., thin-film effects or waveguide resonances) provide comparable current generation in both subcells. However, this optimization must also search for favorable absorber thicknesses, as these parameters will play a key role in defining the total absorption in each subcell and the current mismatch in the device.

The complexity of photon harvesting in ASTRAL can be studied by first building a basic model of the photocurrent that is generated in the cell (see Section 8.4). The model considers ASTRAL as a stack of InGaP and GaAs on a perfect mirror, and assumes that all the incident sunlight is coupled into the stack. The photocurrent generated in each semiconductor layer can then be calculated for a number of absorption cycles $N$ of light through the cell (Figure 3a). In each cycle, light undergoes three steps that subsequently attenuate the field: 1) single-pass absorption in the InGaP, 2) double-pass absorption in the GaAs, and 3) further single-pass absorption in the InGaP (no reflection is considered at the InGaP/GaAs interface). By adding the photocurrent contributions of all cycles, the total photocurrent in each semiconductor layer can be estimated ($J_{sc,InGaP}$ and $J_{sc,GaAs}$), which then

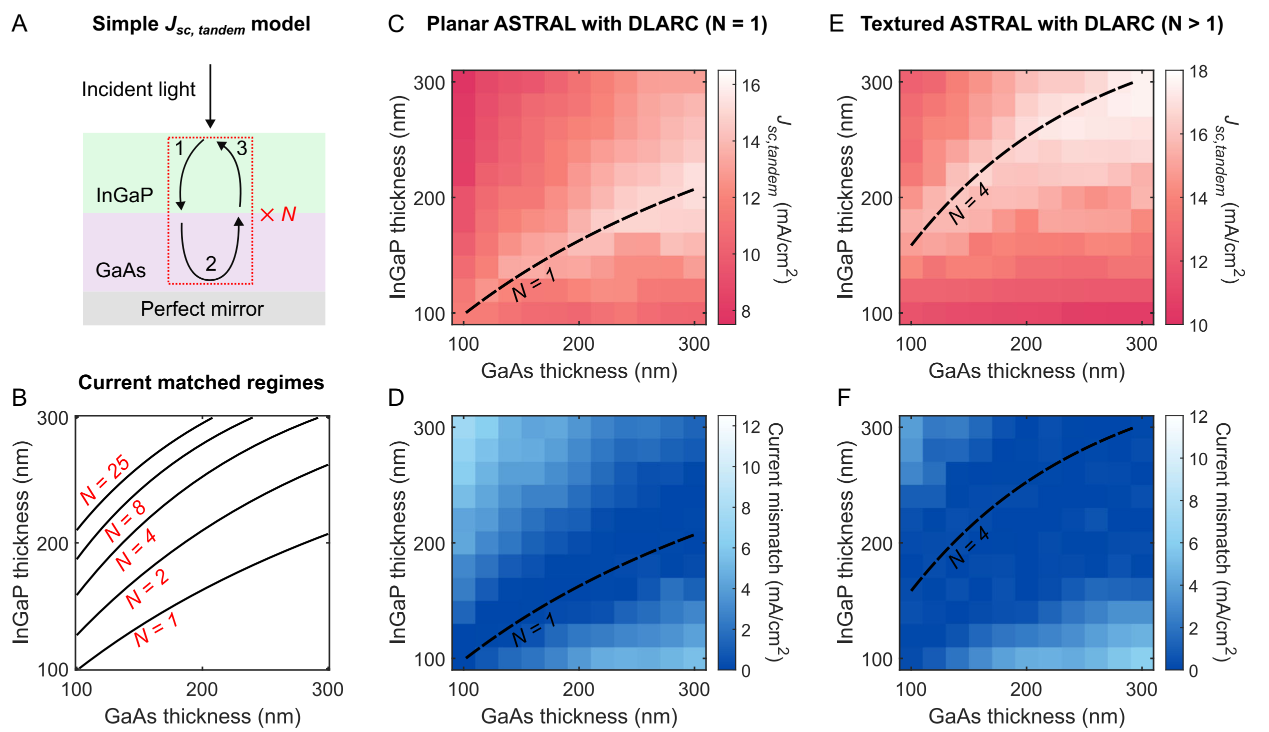


**FIGURE 3** | The photocurrent and current mismatch in an ultra-thin tandem is strongly dependent on the absorber thicknesses and integrated light management. (A) The photocurrent trends in ASTRAL can be studied with a simple Beer–Lambert model that accounts for light absorption through consecutive cycles ($N$) in a simplified tandem cell. (B) For different $N$ values (i.e., different light management strategies achieving varied extension of the optical pathlength in the device), the simple model predicts current matched regimes where the selection of top and bottom cell thicknesses leads to the maximal photocurrent in the cell. (C–F) The trends in the simple model are replicated by full-field simulations of the photocurrent and current mismatch in the full ASTRAL device (Figure 1a), considering both a planar (no texture) and textured configuration. The current matched regime in the planar case follows $N = 1$, and that of the textured device follows $N = 4$. Texture designs in (E,F) correspond to that in Figure 1 with a pitch (unit cell length) of 1.565 μm and optimal thicknesses that vary between 50 and 300 nm.

allows the photocurrent of ASTRAL ($J_{sc,tandem}$, equal to that of the limiting subcell) and the current mismatch ($|J_{sc,InGaP} - J_{sc,GaAs}|$) to be obtained. This simple photocurrent model accounts for the effect of subcell thickness, which determines the absorption in each cycle, as well as for the integrated light-management strategy, which will determine the number of effective cycles of light through the cell. More specifically, a planar cell with an antireflection coating and a rear mirror would correspond to $N = 1$, whereas higher values of $N$ would correspond to cells with additional light-trapping textures. The increment in cycles will depend on the quality of the integrated texture, namely its capacity to prevent outcoupling losses by scattering the incident field outside the escape cone and coupling it to optical modes with high confinement in the absorber layers.

The results of this model are shown in Figure 3b for different cycles of light through the ultra-thin tandem, spanning from $N = 1$ (a double pass) to $N = 25$ (comparable to the Lambertian limit for GaAs). Curves represent the absorber thickness combinations where the model predicts perfect current matching conditions in the cell. In all cases, these current matched regimes are also those absorber thickness combinations offering the highest $J_{sc,tandem}$ for a given $N$. Deviations from these regimes lead to excess current being generated in one semiconductor layer and a loss of current in the other due to the coupling of both absorbers, ultimately dropping $J_{sc,tandem}$. The dependence of device performance on the absorber thickness selection and the integrated light management strategy is evident from the model, as the current matched regime gets displaced for higher $N$ values. This displacement occurs given that the absorption enhancement from light management primarily benefits the bottom cell: as $N$ increases, the absorption enhancement in the bottom cell exceeds that in the InGaP, and so a thicker top cell is required to maintain current matching conditions for a fixed GaAs thickness. Although light management can increase the absorption of photons close to the InGaP bandgap (which are not fully harvested in the ultra-thin top cell), these photons also have appreciable absorption in the GaAs layer and this limits the benefits of the texture for the top cell. Finally, note that as the number of cycles increases and photon harvesting approaches completion, the corresponding displacement of the current-matched regime becomes progressively smaller.

The validity of our simple model is supported by comparing its results against the photocurrent trends of the complete ASTRAL device as in Figure 1a, calculated with full-field electromagnetic simulations. To begin, we model the trends in $J_{sc,tandem}$ (Figure 3c) and current mismatch (Figure 3d) of a planar ASTRAL cell (without a texture) with optimal antireflection in the visible range. For simplicity, in this comparison we consider a double-layer ARC ($MgF_2/Ta_2O_3$) instead of the MFC. For different InGaP/GaAs thickness combinations, we optimize the double-layer antireflection coating (DLARC) by searching for those $MsF_2/Ta_2O_3$ thicknesses that minimize the current mismatch whilst maximising the photocurrent (see Section 8.5). The results of these full-field simulations are in good agreement with our simple model for $N = 1$, as regions of maximal $J_{sc,tandem}$ and minimal current mismatch follow the current-matched regime found by our model. Note that the region with minimal current mismatch is broad in Figure 3d as a consequence of our optimization algorithm, where current mismatch can be alleviated by varying the DLARC thickness to suppress excess absorption in either subcell (by increasing front surface reflection at the relevant wavelengths).

Next, we model the trends in $J_{sc,tandem}$ (Figure 3e) and current mismatch (Figure 3f) of a complete ASTRAL cell with optimal antireflection and light trapping in the visible range. The texture design for this comparison is chosen from previous work [32] and is that shown in Figure 1a with a pitch (unit cell length) of 1.565 μm. For simplicity, we once again consider a $MgF_2/Ta_2O_5$ DLARC and do an optimization for different InGaP and GaAs thickness combinations, in each case searching for those thicknesses of the DLARC and the texture that maximise $J_{sc,tandem}$ whilst minimizing the current mismatch (see Section 8.5). The trends obtained from these simulations are in good agreement with our simple model for $N = 4$, indicating that the integrated texture achieves an eightfold extension of the effective optical pathlength in ASTRAL (considering the entire visible spectral range). Although other light-trapping textures may unlock further pathlength enhancement, approaching the Lambertian limit for all relevant wavelengths is a challenging prospect in realistic device architectures. Note that the thickness regime with minimal current mismatch is broader in Figure 3f compared to Figure 3d, as in the textured case the optimization algorithm has an additional parameter (i.e., texture thickness) that can be adapted to alleviate the current mismatch.

The results presented in this section reveal the dependence that the photocurrent of a two-terminal ultra-thin tandem has on the subcell thickness selection as well as the integrated light management strategy. In ASTRAL, the back reflector and light-trapping texture predominantly benefit the bottom cell. Ultimately, the benefits of these light-management techniques on the absorption of each subcell will depend on the interplay between the thickness and absorption coefficient of the semiconductors under consideration. More importantly, our findings indicate that ASTRAL can achieve longevity on SBSP-relevant orbits and drastic shielding mass reductions without compromising light harvesting. Despite its highly reduced length-scale, the photocurrent in ASTRAL can reach $J_{sc,tandem}$ values of 15–18 mA/cm$^2$ (AM0) that are highly competitive against state-of-the-art InGaP/GaAs tandems, where bottom cells are 10× thicker and $J_{sc,tandem}$ is in the order of 12–14 mA/cm$^2$ (AM1.5G) [20–24, 58]. Additionally, it is important to highlight that the competitive $J_{sc,tandem}$ and current mismatch of ASTRAL remain stable until the end of its lifetime, given that up to this point the photocurrent profile of ultra-thin devices is flat upon radiation exposure [16, 17]. This is a key benefit compared to standard thick tandems, where the photocurrent in each subcell degrades progressively throughout device lifetime with detrimental consequences to the current mismatch.

## 5 | Holistic Optimization of Thermal, Radiation, and Light Management

We now present a specific ASTRAL design where longevity, light management, and thermal management are holistically optimized. For longevity, we focus on a bottom cell thickness of 100 nm, which was found to enable decades-long lifetimes in

SBSP-relevant orbits (Section 3). For light management, we select a top cell thickness of 180 nm and the same light-trapping texture as the one studied in Figure 3, which together were found to enable good current matching and high photocurrent in our tandem at a GaAs thickness of 100 nm (Section 4). For thermal management, the aim is to integrate an MFC design that can enable strong thermal emissivity (equivalent to absorption by Kirchoff's law) in the IR range ($\lambda = 2.5$–$25\ \mu m$), all whilst providing good antireflection at visible wavelengths ($\lambda = 250$–$900$ nm).

We design the MFC by following a two-step optimization process (see Section 8.6). In the first step, we identify a range of favorable MFC designs within a vast parameter space by considering a simplified solar cell structure below the front coating, consisting of a planar stack of InGaP and GaAs on a back reflector. The implemented algorithm has freedom to build the MFC with any of the dielectrics of interest (i.e., $SiO_2$, SiN, $Ta_2O_5$, and AZO), and is able to vary the total number of layers as well as their specific thicknesses (within a maximum limit of 2 μm for the total thickness). The figure of merit in this optimization step aims to maximize the visible absorption in the subcells as well as the emissivity of the coating in the IR regime. In the second step of our optimization process, promising MFC designs from the first step are implemented into the full-textured ASTRAL structure, and their layer thicknesses further optimized within a narrower range to ensure that a high photocurrent and negligible current mismatch are preserved. Implementing these two steps allows to search a broad parameter space for the MFC whilst reducing the computational demand for the optimization, as planar designs allow for less intensive simulation methods than their textured counterparts.

The output of the first optimization step consisted of a library of coatings with different metrics for the visible absorption in the tandem cell and IR emissivity (see Figure S1, Supporting Information). Generally, this library can be divided into MFC designs with and without AZO in their layer structure. The visible absorption in the tandem cell was comparable for both categories. However, those designs with AZO were found to enable superior IR emissivity in all cases, as this material enables wider spectral emission bands down to $\lambda \approx 2\ \mu m$, compared to our other materials of interest where emission drops at $\lambda \approx 7$–$10\ \mu m$. Additionally, the number of layers ($L$) in the coatings was not found to have a significant impact on their performance, as high metrics were already observed for those AZO-free designs at $L = 3$, and at $L = 4$ for AZO-containing designs. In both cases, these high-performing low-$L$ MFCs contained one layer of each of the available dielectrics.

From the output of this first optimization step, we selected 2 high-performing designs with low $L$ (one with AZO, one without) to integrate into the complete ASTRAL structure. After carrying out the second optimization step with these coatings, we obtained final designs labelled MFC (AZO) and MFC (AZO-free). Their layer structure, as well as the absorption/emission profiles resulting after their integration into ASTRAL, are shown in Figure 4ab. Key metrics for these designs are included in Table 1.

The results highlight the success of our optimization algorithm in delivering MFC designs that lead to high photocurrent ($\sim$14 mA/cm$^2$) and IR emissivity (>60% assuming a device temperature of 100°C) as well as negligible current mismatch (<0.01 mA/cm$^2$). For comparison, space-qualified coverglass can offer emissivity $\simeq$80% [59], which is comparable to MFC (AZO) but entails orders-of-magnitude increments in mass. The benefits of the AZO for the IR emissivity are evidenced in the enhanced absorption of MFC (AZO) in this spectral range. As shown in Table 1, the total emissivity in the IR for MFC (AZO) is 79% at 100°C, surpassing that of MFC (AZO-free) by 16%. However, the photocurrent of MFC (AZO-free) is higher than that of MFC (AZO), given that the AZO introduces more parasitic absorption of sunlight and limits the transmission of photons to the underlying cell. As shown in Table 1, the parasitic absorption of the coating in MFC (AZO) exceeds that of MFC (AZO-free) by 4% in the visible range ($\lambda = 250$–$900$ nm).

For comparison, we present absorption/emission profiles of complete ASTRAL devices with a standard $SiO_2$/$Ta_2O_5$ DLARC (Figure 4c) and no front coating (Figure 4d). These designs were obtained by directly following the second optimization step of our algorithm. A DLARC enables a higher $J_{sc,tandem}$ of 15.4 mA/cm$^2$ due to its reduced parasitic absorption in the visible range, which is $\sim$10% lower than that of the MFCs (see Table 1). The main driver of this reduction in parasitic absorption is the total coating thickness, which is $\sim$2 μm for the MFCs and only 150 nm for the DLARC. However, the benefits of our MFCs over a standard DLARC are clear in the IR regime, where the latter shows an extremely poor emissivity of 6% (Table 1). For the case where ASTRAL has No coating, the IR emissivity is negligible (<1%) and $J_{sc,tandem}$ suffers a considerable penalty from the lack of antireflection at visible wavelengths, decreasing to 10.7 mA/cm$^2$. Additionally, despite remaining low, it is worth highlighting that the current mismatch in the DLARC and No coating designs is higher than in the MFCs. This is a result of the optimization algorithm, as the MFCs have more variables that can be adapted to minimize the current mismatch (i.e., more layer thicknesses in the coating). Finally, note that both the DLARC and No coating designs would also suffer from reduced shielding from low-energy particles, leading to reduced on-orbit longevity. In the end, it is our MFC designs that couple decades-long lifetimes on SBSP orbits with a competitive photocurrent, minimal current mismatch, and high emissivity in the IR for thermal management.

## 6 | Photovoltaic Efficiency and Operating Temperatures of ASTRAL

Previous sections introduced a framework to optimize the design of ASTRAL toward radiation tolerance in hostile space environments, competitive photocurrent and current matching, and high IR emissivity for thermal management. We now estimate the operating temperature and photovoltaic efficiency of our optimal designs under varying levels of concentration. Given its relevance for SBSP, we focus on operation in a GEO environment.

We start by building a model of the power flux in ASTRAL (Figure 5a, see Section 8.7). As the system design where ASTRAL would be integrated is not yet defined, this model is only representative. The model considers the structural support of ASTRAL as a blackbody and assumes perfect thermal contact between all system components. Input power in the system is

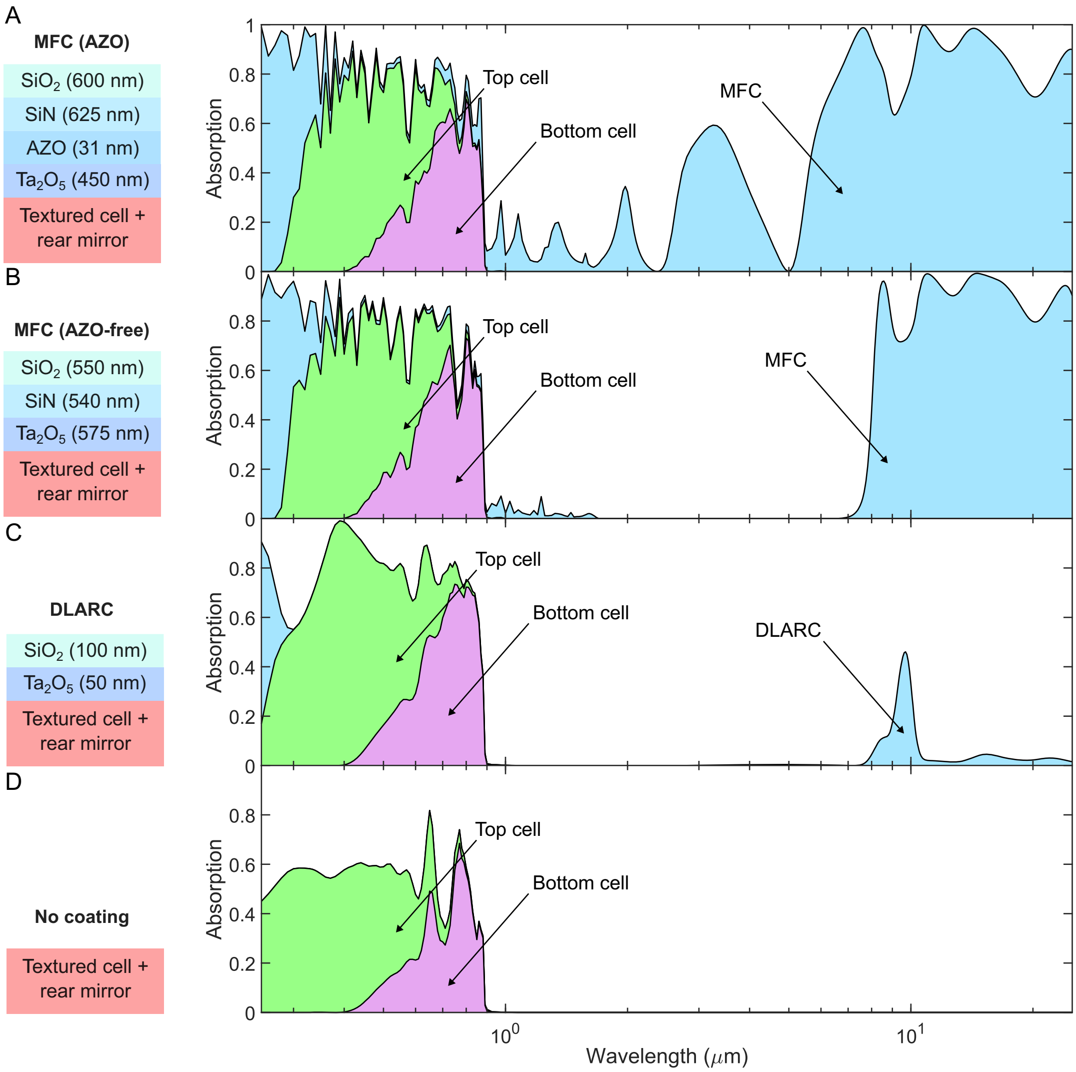


**FIGURE 4** | ASTRAL can be designed to couple longevity in space orbits as well as efficient light and thermal management. A representative ASTRAL structure is proposed based on the results of Sections 3 and 4, with absorber thicknesses of 180 nm (InGaP) and 100 nm (GaAs) and the texture design in Figure 1. Collectively, these selections enable decades-long lifetimes on SBSP orbits and favorable light harvesting. (A,B) From these starting conditions, MFC designs are optimized with a view to maximizing antireflection in the visible range and absorption/emissivity in the IR. (C,D) Results for ASTRAL devices with a standard double-layer antireflection coating (DLARC) and No coating are also included. Key metrics of these designs are shown in Table 1, highlighting the competitive photocurrent, high IR emissivity, and negligible current mismatch enabled by our MFC desings. In all cases the pitch (unit cell length) of the texture is 1.565 μm, whereas optimal texture thicknesses are 100 nm (A,B), 125 nm (C), and 150 nm (D).

**TABLE 1** | Key metrics for the ASTRAL designs in Figure 4.

| Metric | MFC (AZO) | MFC (AZO-free) | DLARC | No coating |
|---|---|---|---|---|
| $J_{sc,tandem}$ at 1 sun (AM0, mA/cm$^2$) | 13.8 | 14.2 | 15.4 | 10.7 |
| Current mismatch at 1 sun (AM0, mA/cm$^2$) | 0.004 | 0.006 | 0.163 | 0.175 |
| IR emissivity at 100°C (%) | 79 | 63 | 6 | 0.4 |
| Integrated visible absorption in coating (%) | 15 | 11 | 2 | 0 |
| Integrated near-IR absorption in coating (%) | 77 | 68 | 4 | 0 |

assumed to be independent of temperature and consists of the solar absorption from the front surface of ASTRAL (obtained from those results in Figure 4), as well as the absorption of Earth's blackbody emission by the structural support (considering the corresponding solid angle on GEO). Output power is temperature-dependent and consists of the emission by the front coating (modeled as a graybody with the emissivity obtained in Figure 4), the emission by the structural support, and the electric power generated by the cell (calculated from a detailed balance model taking the appropriate absorption profiles in Figure 4). For

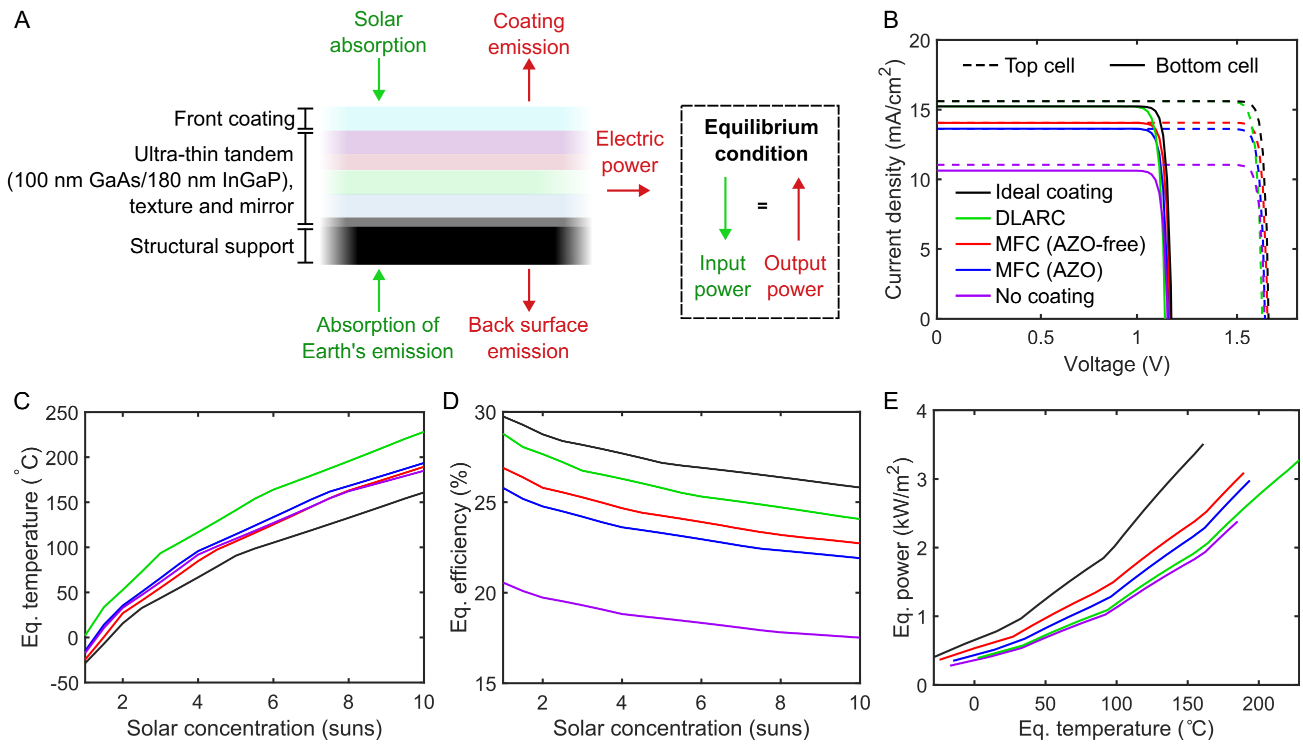


**FIGURE 5** | ASTRAL can produce electric power on the kW/m$^2$ scale at regulated temperatures <100°C, thus being a competitive PV technology to deliver GW-scale SBSP. (A) Representative diagram of the power flux in ASTRAL, showing input and output sources. (B) Representative LIV curves of all designs in Figure 4 at equilibrium conditions under 1 sun illumination, calculated with a detailed balance model. The equilibrium temperature and photovoltaic efficiency of these designs are included in (C,D) as a function of solar concentration. The change in electric power output as a function of the operating temperature is shown in (E).

simplicity, we do not account for the emission by the subcells (and, by extension, radiative coupling) as this term has small contributions and does not change trends considerably (additionally, note that our ultra-thin subcells are unlikely to harvest a considerable fraction of the radiated power). It is worth highlighting that specific system designs may deviate from our representative model, either due to their specific geometry (e.g., a standard paddle arrangement versus a tile design [42, 43, 60]) or to temporal changes (e.g., satellites passing through Earth's shadow). These exact deviations should be analyzed on a case-by-case basis and are outside the scope of this work.

In our power flux model, the system reaches equilibrium when the temperature of the system is such that the total output power matches the total input power. This equilibrium temperature, together with the corresponding photovoltaic efficiency, is included in Figure 5c,d for all the designs presented in Figure 4, namely MFC (AZO), MFC (AZO-free), DLARC, and No coating. Results are shown as a function of concentration up to 10 suns, which is achievable with ultra-lightweight concentration systems that employ reflective optics and are compatible with ASTRAL [42, 43]. Representative IV curves under 1 sun illumination are also included for all designs in Figure 5b, obtained with our detailed balance model.

Generally, our model indicates that increasing concentration leads to an increase in operating temperature due to the higher input power in the system (Figure 5c). Owing to its low IR emissivity and high absorption of solar power, the DLARC has the highest operating temperature of all designs, starting at ∼0°C without concentration and increasing to ∼240°C at 10 suns. MFC (AZO), MFC (AZO-free), and No coating all have lower and comparable temperatures, starting at ∼−20°C without concentration and increasing to ∼190°C at 10 suns. The comparable temperatures among these three designs are driven by different effects. For the No coating case, the absence of antireflection leads to less solar illumination being absorbed in the system (i.e., lower input power), which limits the temperature increase in the device despite its negligible radiative cooling properties. For both our MFC designs, the absorbed solar power is considerably higher (as evidenced by their higher photocurrent), but the emission of power by the coating is sufficient to keep operating temperatures to a similar level than the No coating case. Additionally, it is worth highlighting that the difference in IR emissivity (Table 1) between MFC (AZO) and MFC (AZO-free) does not lead to a considerable difference in operating temperature, and it is, in fact, MFC (AZO-free) which operates at a lower temperature despite its lower IR emissivity. This phenomenon was found to be a consequence of the parasitic absorption in the coatings: whilst MFC (AZO) does emit more power, it also absorbs more power in both the visible and near-IR regimes (Table 1), and so the balance of input and output power ends up being comparable (and even slightly more detrimental) to MFC (AZO-free).

Our model also reveals that ASTRAL can reach photovoltaic efficiencies exceeding 25% at 1 sun, competitive against state-of-the-art InGaP/GaAs tandems [20, 21, 23, 24, 58, 61]. A ∼3%–4% reduction in efficiency is observed in all designs as concentration increases to 10 suns, which is due to the corresponding increment in operating temperature. In particular, it was found that the change in efficiency as a function of temperature followed a mostly linear behavior in all designs, varying slightly within the 1–10 suns range and staying around −0.02 to −0.03% $K^{-1}$ (see Figure S2, Supporting Information). This temperature penalty is on the same order of magnitude as experimental results reported in the literature for single [62] and multijunction III–V cells [58, 63, 64]. On the contrary, the concentration benefits to the efficiency were found to follow an inverse relationship, generally varying within 0.1–0.4% $suns^{-1}$ in the 0°C–250°C range and being more significant for hotter devices (see Figure S3, Supporting Information). Ultimately, at the equilibrium conditions in Figure 5 the temperature penalty on the efficiency outweighs the benefits of concentration.

Despite its higher operating temperature, the efficiency of the DLARC outperforms all other designs. This is a consequence of the higher $J_{sc,tandem}$ in this system. At the equilibrium conditions in Figure 5, the change in the efficiency of the tandem as a function of the photocurrent value at 1 sun is in the order of ∼1.6–1.85% $mA^{-1}cm^2$ (see Figure S4, Supporting Information). The DLARC design has a $J_{sc,tandem}$ that outperforms other designs by at least 1 $mA/cm^2$ at 1 sun (Table 1), and so the corresponding efficiency gain is not outweighed by the detriments of its higher temperature, which is at most ∼40°C hotter for all solar concentration values shown in Figure 5. At equilibrium conditions, the prominence of $J_{sc,tandem}$ for the photovoltaic efficiency is further evidenced by the ranking of different designs in Figure 5c, which follows the same ranking as the photocurrent in Table 1.

Fundamental device efficiency, calculated using detailed balance, only gives a partial picture of anticipated device performance, with elevated temperatures also introducing significant engineering challenges and further extrinsic losses. The exceptional potential of ASTRAL for SBSP is demonstrated in Figure 5e, which shows the generated electric power as a function of the operating temperature for different system designs. Generally, ASTRAL can deliver electric power in the order of $kW/m^2$ under low concentration, which is well-suited to meet the demands of current SBSP stations designed to generate GW-level power with km-scale PV [7]. Furthermore, these results clearly expose the benefits of our MFC designs. It is evident that both MFC (AZO) and MFC (AZO-free) outperform the standard DLARC and the No coating case, in all cases generating more power at a given temperature. In particular, MFC (AZO-free) produces ∼25%–35% more power than the standard DLARC in the ∼10°C–150°C temperature range, and is capable of generating 1 $kW/m^2$ at 50°C. The ability to deliver more electric power for a given temperature is more relevant than absolute efficiency trends, as maintaining low operating temperatures is essential to preserve system lifetime. For example, beyond certain temperature thresholds bonding materials may deteriorate, or metal contacts may diffuse to the ultra-thin absorber layers and shunt the device, potentially leading to system failure [65]. Other temperature effects that can compromise system performance include dopant difussion, structural degradation of the array, or breakdown of the semiconductor materials themselves [66]. Ultimately, the MFC designs presented here produce the highest output power for a fixed temperature threshold.

Finally, it is worth highlighting other strategies that could be implemented to further reduce the operating temperature of ASTRAL. First, the system could be thermally coupled to a radiator [13]. This strategy would effectively increase the power output per unit area in the system, thus driving a reduction in the equilibrium temperature. Provided that a good radiator can be integrated with high IR emissivity and minimal absorption in the visible and near-IR regimes, the operating temperature of ASTRAL with MFC (AZO-free) could drop to 100°C at 10 suns for a radiator of equal size to the solar cell, generating power in excess of 3 $kW/m^2$ (see Supporting Information Discussion 1). A different strategy to reduce the operating temperature would be to design MFCs with materials that hold superior optical properties to the ones considered in this work. An ideal MFC would have zero absorption in the visible and near-IR regimes, and complete absorption/emission at IR wavelengths. Assuming such properties are obtained in a coating that enables the same absorption in the subcells as the DLARC design, a clear improvement is observed in the equilibrium temperature, efficiency, and power output ('Ideal coating', black line in Figure 5c–e). In practice, approaching these ideal properties with our MFCs is limited by fundamental material properties (i.e., emission bands), but further research could reveal novel coating candidates with more suitable optical characteristics.

To conclude, our rigorous modeling work demonstrates that ASTRAL can produce electric power in excess of 1 $kW/m^2$ at temperatures below 100°C, all whilst having a deployable design with remarkable radiation tolerance and ultralow weight, able to survive for decades on a GEO orbit with >30× reduction in shielding mass and corresponding launch costs. The synergy of these properties makes ASTRAL a powerful and unique candidate to deliver SBSP.

## 7 | Conclusions

SBSP is positioned as a compelling technology for the energy transition, with the potential to deliver continuous, clean, and affordable baseload energy to our planet on the GW-scale.

Here we present ASTRAL, a unique PV concept conceived to accelerate the dawn of SBSP. Our ultra-thin InGaP/GaAs tandem solar cell couples key criteria for the delivery of solar energy from space, namely high radiation tolerance, ultra-low weight and high specific power, flexible form factors, and reduced component costs. The potential of this design is revealed by means of rigorous modeling spanning across radiation, optical, and thermal device simulations.

More specifically, we demonstrate that ASTRAL can survive in space without the need for conventional heavy coverglass (∼100 μm) for radiation shielding. Instead, owing to the intrinsic and remarkable radiation tolerance of its ultra-thin (∼100–200 nm) absorber layers, only 2 μm of protective dielectric coating are sufficient to enable a system lifetime in the order of decades on a geostationary orbit. The corresponding >30× reduction in shielding mass entails a proportional drop in launch costs, which could represent savings of hundreds of millions of dollars for the kilometer-scale stations that are currently envisioned for SBSP. Our coverglass-free embodiment deviates from current paradigms in space PV and unlocks flexible form factors for the solar arrays to improve deployability. Furthermore, we expect this coverglass-free embodiment to be protected from UV damage by the 2-μm thick dielectric front coating, and to have sufficient structural support from its lightweight flexible substrate.

Additionally, we show that ASTRAL can provide a high-power output > 1 kW/m$^2$ under low concentration (<10 suns) and at operating temperatures below 100°C. These properties are achieved by carefully optimizing the device layer structure towards a high photocurrent, negligible current mismatch, and high IR emissivity for passive radiative cooling under concentration in space. For the photocurrent, in our ultra-thin tandem the integration of light management is essential to boost the otherwise low absorption of photons. The particular strategy that we study in this work is the integration of a rear mirror and a quasi-random light-trapping texture. We demonstrate that the quality of the integrated light management, namely the effective extension of the optical path length in the device, dictates the most favorable absorber thickness selection to unlock the highest photocurrent with minimal current mismatch. For the IR emissivity, we demonstrate that this property can be coupled with the radiation shielding and antireflection properties of the dielectric front coating of the system. In particular, we show that the best coatings for radiative cooling are those with high emission in the IR and negligible absorption in the visible and near-IR regimes, as this parasitic absorption increases the input power in the system and is detrimental to the electric power output.

Finally, the optimization framework presented in this work achieves thermal, radiation, and light management in a single ultralow weight solar cell. As a result, we present a unique PV technology that couples all the key functionalities to deliver clean energy from space in a system that is compatible with current SBSP station designs.

## 8 | Methods

### 8.1 | On-Orbit Differential Particle Fluxes

Simulation of the differential particle fluxes encountered on Molniya, GEO and Phase 1 Starlink (LEO) orbits was carried out using SPENVIS [47]. The radiation models used were the AE9/AP9 models of IRENE, version 1.50, which was run in mean mode.

### 8.2 | Particle Stopping Distance

The range of energetic protons in CMG coverglass and the dielectric materials comprising the MFC were simulated using the stopping and range of ions in matter (SRIM) software [67]. The range of electrons in these materials was estimated using CASINO [68].

### 8.3 | Estimation of Time to Short-Circuit Current Collapse

It has previously been shown that the radiation-induced short-circuit current degradation in ultra-thin solar cells occurs over a narrow fluence range (i.e., there is a collapse in short-circuit current). This $J_{sc}$ collapse can be attributed to the degradation in absorber layer carrier lifetime ($\tau$) below the transit time ($t_{\mathrm{tr}}$), which is the time taken by carriers to transit across the absorber layer [17]. If both the variation of carrier lifetime with radiation fluence ($\Phi_r$) and the transit time are known, the fluence at which short-circuit current degradation occurs can be estimated.

To demonstrate this in a generalized model that allows for any radiation type (or a radiation spectrum instead of monoenergetic radiation), we work with the displacement damage dose (DDD) instead of radiation fluence. DDD is a measure of the energy deposited by incident radiation in a target through non-ionising processes, namely the displacement of atoms/ions. It can be defined for both monoenergetic radiation of energy $E_0$ and for a spectrum of radiation energies ($E$) ranging from $E_{\mathrm{min}}$ to $E_{\mathrm{max}}$.

$$\mathrm{DDD} = \mathrm{NIEL}(E_0)\Phi_r(E_0) = \int_{E_{\mathrm{min}}}^{E_{\mathrm{max}}} \mathrm{NIEL}(E)\frac{d\Phi_r(E)}{dE}dE \quad (1)$$

where NIEL is the non-ionising energy loss, which depends on the radiation particle type, radiation energy and target material [46, 69]. In this work, NIEL is calculated using the INFN SR-NIEL calculator in SPENVIS [47], using the threshold displacement energies given by Jun et al. [70]. The benefit of using DDD is that it is a measure of the extent of radiation damage induced in a target, which is independent of the radiation type used.

Carrier lifetime is known to degrade with DDD according to

$$\frac{1}{\tau} = \frac{1}{\tau_0} + K_\tau \mathrm{DDD} \quad (2)$$

where $K_\tau$ is the lifetime damage constant and $\tau_0$ is the pre-irradiation lifetime. These parameters can be obtained by fitting this model to experimental data of carrier lifetime in the absorber layer post-irradiation to a range of fluences. This was done previously for ultra-thin solar cells with 80 nm thick GaAs absorber layers irradiated with 3 MeV protons, measuring lifetime using time-resolved cathodoluminescence (TRCL) [17].

The transit time in the absorber layer of an ultra-thin solar cell can be calculated from the equation for drift velocity (Equation 3), when the layer is fully depleted and carrier transport is dominated by drift:

$$v_{\mathrm{drift}} = \frac{dx}{dt} = \mu F(x) \quad (3)$$

where $\mu$ is the carrier mobility and $F(x)$ is the position-dependent electric field. In this study, the field is calculated using the Solcore Poisson drift diffusion (PDD) solver [15].

Equation (3) can be rearranged to give Equation (4) for the transit time, in which the integral is taken over the entire width of the absorber layer, as indicated by $W$.

$$t_{\mathrm{tr}} = \frac{1}{\mu}\int_W \frac{dx}{F(x)} \tag{4}$$

Different carrier types tend to have different mobilities and lifetimes in semiconductors. This study uses carrier lifetime measured by TRCL, which does not distinguish between electrons and holes. The assumption is made that this is representative of the lifetimes of both carriers. Given this assumption, the carrier with the lowest mobility, and therefore the greatest transit time, is anticipated to initiate the degradation in short-circuit current, as the carrier lifetime will reach this transit time first. In GaAs, holes have a lower mobility than electrons. The value of hole mobility used in this study is the low-doping limit of 490 $\mathrm{cm^2\ V^{-1}\ s^{-1}}$ [71], given that the absorber layer is assumed to be fully depleted.

So far, the degradation of short-circuit current has only been attributed to carrier lifetime degradation, but another factor that should be taken into consideration is carrier removal. Carrier removal occurs as a result of the introduction of defects by radiation, which can act as majority carrier traps, reducing the free carrier concentration in the device. This alters the junction's band structure and the electric field $F(x)$ across it, resulting in a change in the transit time. The process of carrier removal can be quantified by Equation (5) [72],

$$n(\mathrm{DDD}) = n_0 \exp\left(\frac{-R_c\mathrm{DDD}}{n_0}\right) \tag{5}$$

where $R_c$ is the carrier removal rate, $n_0$ is the initial carrier concentration and $n(\mathrm{DDD})$ is the fluence-dependent carrier concentration.

With established relationships for the variation of both lifetime and transit time with DDD, the critical DDD ($\mathrm{DDD}_c$) at which the short-circuit current is expected to degrade can be determined. $\mathrm{DDD}_c$ is the fluence at which the following condition is met.

$$\tau(\mathrm{DDD}_c) = t_{\mathrm{tr}}(\mathrm{DDD}_c) \tag{6}$$

$\mathrm{DDD}_c$ can be converted into a duration on a specific orbit if the DDD rate for that orbit is known. In this study, the DDD rate is given by the annual DDD ($\mathrm{DDD}_a$), calculated using MULASSIS [73] and the IRENE AE9/AP9 radiation models (in *mean* mode) [74] in SPENVIS [47]. MULASSIS also allows the effect of radiation shielding to be considered, which alters the radiation spectrum incident on the target and therefore the $\mathrm{DDD}_a$.

Using $\mathrm{DDD}_c$ and $\mathrm{DDD}_a$, the longevity of an ultra thin solar cell on a specific orbit, in years, is given by:

$$\text{Longevity on orbit in years} = \frac{\mathrm{DDD}_c}{\mathrm{DDD}_a(\text{orbit})} \tag{7}$$

Finally, note that a specific GaAs subcell structure was required in order to apply this model to study the effect of absorber layer thickness on longevity (Figure 2c). This is because the longevity is affected by the bandstructure of the subcell, which not only depends on the doping in the absorber layer, but also on that of the passivation layers. The structure chosen, given in Table 2, is representative and based on previously studied ultra-thin GaAs devices, for which carrier lifetime degradation data is available [17]. In previous studies, the absorber layer thickness ($W$) was fixed at 80 nm, but in this study it is allowed to vary between 80 and 200 nm. Beyond 200 nm, the assumption used in the model of carrier transport being dominated by drift begins to break down, since thicker devices will not be fully depleted. While carrier lifetime data is only available for devices with $W = 80$ nm, the assumption is made that the lifetime damage constant ($K_\tau$) of the GaAs absorber layer does not vary with its thickness. This is reasonable, as $K_\tau$ depends on the defect introduction rate and carrier capture cross-sections of defects, which are unlikely to be affected significantly by layer thickness.

Given the structure in Table 2, the values of $R_c$ used in this study (calculated from measurements by Sato et al. [48]) are $1.3 \times 10^5$ g $\mathrm{MeV^{-1}\ cm^{-3}}$ for InGaP and $2.1 \times 10^5$ g $\mathrm{MeV^{-1}\ cm^{-3}}$ for GaAs. No published values for the $R_c$ of InAlP were found. In order to provide an estimate of the effect of carrier removal, a value of $R_c$ needed to be assigned to InAlP and was chosen to be the same as that for InGaP. It is likely that the $R_c$ of InAlP would be more similar to that of InGaP than GaAs, as InAlP and InGaP are both alloys of InP.

### 8.4 | Simple Photocurrent Model for ASTRAL

Our simple model of light harvesting in ASTRAL estimates the photocurrent generated in each semiconductor layer ($J_{sc,InGaP}$ and $J_{sc,GaAs}$), assuming that the incident photon flux ($\Phi$) is absorbed and attenuated in a number of cycles $N$ of incident light through an InGaP/GaAs stack placed on a perfect mirror. In each cycle, the consecutive absorption events are i) single-pass absorption in the InGaP ($A_1$), ii) double-pass absorption in the GaAs ($A_2$), and iii) further single-pass absorption in the InGaP ($A_3$). The photocurrents are calculated as

$$\begin{aligned} J_{sc,InGaP} = q\sum_{n=1}^{N}\Bigg[&\int_a^b A_1(\lambda)\Phi_{n-1}(\lambda)\,d\lambda \\ &+ \int_a^b A_3(\lambda)\Phi_{n-1}(\lambda)(1-A_2(\lambda))(1-A_1(\lambda))\,d\lambda\Bigg] \end{aligned} \tag{8}$$

**TABLE 2** | Representative ultra-thin GaAs subcell structure with doping density and thickness values. The thickness of the absorber layer (W$W$) is a variable.

| Layer function | Material | Doping density ($\mathrm{cm^{-3}}$) | Thickness (nm) |
|---|---|---|---|
| Hole barrier | $\mathrm{In_{0.47}AlP}$ | $5\times10^{18}$ | 20 |
| n-type absorber | GaAs | $1\times10^{17}$ | $W/2$ |
| p-type absorber | GaAs | $1\times10^{17}$ | $W/2$ |
| Electron barrier | $\mathrm{In_{0.49}GaP}$ | $5\times10^{18}$ | 20 |

and

$$J_{sc,GaAs} = q\sum_{n=1}^{N}\int_a^b A_2(\lambda)\Phi_{n-1}(\lambda)(1-A_1(\lambda))\,d\lambda \tag{9}$$

where $q$ is the elementary charge, $\lambda$ is the wavelength, $a$ and $b$ are 250 and 900 nm, respectively, $\Phi_0$ is the incident photon flux (AM0 in this work), and the progressively attenuated photon flux $\Phi_n$ is

$$\Phi_n(\lambda) = \Phi_{n-1}(\lambda)(1-A_3(\lambda))(1-A_2(\lambda))(1-A_1(\lambda)) \tag{10}$$

The absorption in the semiconductors is calculated following a Beer–Lambert model

$$A_{1,3}(\lambda) = 1 - \exp\left(-\alpha_{InGaP}(\lambda)d_{InGaP}\right) \tag{11}$$

and

$$A_2(\lambda) = 1 - \exp\left(-2\alpha_{GaAs}(\lambda)d_{GaAs}\right) \tag{12}$$

where $\alpha$ is the absorption coefficient of the semiconductor under consideration and $d$ its thickness. The optical constants used in our calculations can be found in Supporting Information Discussion 2.

## 8.5 | Optimization of Photocurrent and Current Mismatch with Full-Field Simulations

To maximize the photocurrent and minimize the current mismatch of ASTRAL, we perform an optimization with the following figure of merit $O$

$$O = |J_{sc\,GaAs} - J_{sc\,InGaP}| - J_{sc,\,tandem} \tag{13}$$

where $J_{sc\,InGaP}$ and $J_{sc\,GaAs}$ are the photocurrent generated by the top and bottom cell, respectively, and $J_{sc,\,tandem}$ is the phorocurrent generated by the limiting cell. For each subcell, the photocurrent was calculated as

$$J_{sc} = q\int \Phi(\lambda)A(\lambda)d\lambda \tag{14}$$

where $q$ is the elementary charge, $\Phi$ is the photon flux from the AM0 solar spectrum, and $A$ is the absorption in the corresponding subcell. The absorption is obtained from rigorous coupled-wave analysis (RCWA) simulations of the entire device structure as in Figure 1a (including the barrier layers, tunnel junction, the appropriate front coating, the Ag back reflector, and the integrated texture when relevant). Note that in this work we consider that the absorption in the absorber and barrier layers of each subcell can contribute to the photocurrent (as has been experimentally demonstrated for single-junction 80 nm GaAs devices [19]).

Our optimization method to minimize $O$ is based on a differential evolution algorithm [75]. Optimization parameters vary for different ASTRAL designs but generally consist of front coating layer thicknesses and/or texture thickness. The calculation of $A$ was done with a modified version of the MATLAB-based RCWA implementation GD-Calc [76]. Textured simulations accounted for 225 Fourier orders for convergence. The optical constants used in the RCWA simulations are included in Supporting Information Discussion 2.

## 8.6 | Two-Step Optimization of the MFC in ASTRAL

Both steps of our MFC optimization implemented the optical constants included in Supporting Information Discussion 2.

### 8.6.1 | First Step

We identify favorable MFC designs for a simplified ASTRAL structure, consisting of a planar InGaP/GaAs/Ag stack. The optimization is done with a Python-based genetic algorithm [77]. In our implementation, the algorithm has the freedom to select any of our materials of interest to build the MFC (i.e., $SiO_2$, SiN, $Ta_2O_5$, and AZO) and is able to vary the total number of layers as well as their specific thicknesses [78]. The total thickness of the MFC, however, is set to be in the order of ~2 µm, so as to ensure that this coating can offer some protection from low energy particle damage (see Section 3).

The optimization algorithm aims to maximize the target function $F$

$$F = A_c \times \epsilon \tag{15}$$

where $A_c$ and $\in$ are weighted values of the total visible absorption in the simplified tandem (InGaP + GaAs layers) and the IR emissivity of the entire stack (MFC + underlying cell), respectively, defined by

$$A_c = \frac{\int_{0.3\,\mu m}^{0.9\,\mu m} A_t(\lambda)B(\lambda,T_1)\,d\lambda}{\int_{0.3\,\mu m}^{0.9\,\mu m} B(\lambda,T_1)\,d\lambda} \tag{16}$$

$$\in = \frac{\int_{2.5\,\mu m}^{25\,\mu m} A_t(\lambda)B(\lambda,T_2)\,d\lambda}{\int_{2.5\,\mu m}^{25\,\mu m} B(\lambda,T_2)\,d\lambda} \tag{17}$$

where $B$ is the blackbody emission from Plank's law, calculated at $T_1 = 5777$ K (solar surface temperature) and $T_2 = 373$ K (representative device temperature). $A_t(\lambda)$ is the total optical absorption of the simulated structure, calculated with TMM simulations. Since the TMC materials have low visible absorption, in this spectral range $A_t(\lambda)$ can be considered to mainly originate from the solar cell structure. Note that our optimisations were done with an individual population set of 200 and an evolution generation of 50. The final optimized design is the best candidate at the 50th generation, as at this point good convergence is commonly observed.

### 8.6.2 | Second Step

We integrate promising MFC designs from the first step in the full textured ASTRAL device, and follow the optimization algorithm presented in Section 8.5. The optimized variables in this second step are the thicknesses of each layer in the MFC (except for the AZO), as well as that of the nanophotonic texture. Note that the search for favorable thicknesses for the MFC layers was restricted to about ± 50 nm of those obtained from the first optimization step, and the AZO thickness was fixed to its output value from the first optimization step. These restrictions were implemented to preserve good IR emissivity and prevent the complete elimination of the AZO layer in the second step of the optimization (i.e., zero thickness), as $O$ does not consider $\in$ and the presence of AZO is detrimental for the photocurrent.

## 8.7 | Power Flux Model

We consider that the balance of power in ASTRAL ($P_{flux}$) depends on different input and output sources. Input sources consist of the absorption of solar energy ($P_{solar}$) and the absorption of Earth's emission ($P_{Earth}$). Output sources depend on the temperature of the system ($T_{system}$), and consist of the electric power generated by the cell ($P_{elec}$), the emission by the front surface of the system ($P_{s1}$), and the emission by the back surface of the system ($P_{s2}$). From these considerations, it follows that

$$P_{flux}\left(T_{system}\right) = P_{solar} + P_{Earth} - \Big(P_{elec}\left(T_{system}\right) + P_{s1}\left(T_{system}\right) + P_{s2}\left(T_{system}\right)\Big) \tag{18}$$

ASTRAL reaches equilibrium when $T_{system}$ is such that $P_{flux} = 0$. To find this condition, in this work we solve Equation (18) for a range of values of $T_{system}$ (between 100 and 700 K), and interpolate the equilibrium temperature from the obtained results.

Every term in Equation (18) depends on the photon energy emission flux ($B$) per energy interval ($dE$), which is defined for a blackbody as

$$B(E, T, \Omega) = \frac{2\Omega E^3}{c^2 h^3} \frac{1}{exp(E/(k_B T)) - 1} \tag{19}$$

where $E$ is the photon energy, $c$ is the speed of light, $h$ is Planck's constant, $k_B$ is Boltzmann's constant, $T$ is the temperature, and $\Omega$ is the solid angle subtended by the emitting body.

The energy input from solar absorption is considered to come through the front surface and is modeled as

$$P_{solar} = \int_{E1}^{E2} \chi A_{system}(E) B(E, T_{sun}, \Omega_{sun}) dE \tag{20}$$

where $E1$ is the photon energy at $\lambda = 25$ μm, $E2$ is the photon energy at $\lambda = 250$ nm, $T_{sun}$ is the temperature of the sun (5772 K), $A_{system}$ is the total absorptivity of ASTRAL (subcells + front coating), $\chi$ is the solar concentration (suns), and $\Omega_{sun}$ is the solid angle subtended by the Sun ($6.8 \times 10^{-5}$ sr).

The energy input from the absorption of Earth's emission is considered to take place through the structural support at the rear of ASTRAL. As both the Earth and this structural support are assumed to behave as a blackbody, the corresponding power input from Earth is defined as

$$P_{Earth} = \int_{E1}^{E2} B(E, T_{Earth}, \Omega_{Earth}) dE \tag{21}$$

where $T_{Earth}$ is the temperature of Earth (assumed to be 300 K) and $\Omega_{Earth}$ is the solid angle subtended by Earth on GEO (0.0723 sr).

The emission of the structural support is

$$P_{s2} = \int_{E1}^{E2} B\left(E, T_{system}, \pi\right) dE \tag{22}$$

The emission by the front surface of the cell is

$$P_{s1} = \int_{E1}^{E2} A_{coating}(E) B\left(E, T_{system}, \pi\right) dE \tag{23}$$

where $A_{coating}$ is the absorptivity/emissivity of the front coating.

Finally, the power generated by the solar cell is obtained from a detailed balance model. The current–voltage characteristics of each subcell $i$ in the tandem are

$$J_i = q \int_{E1}^{E2} \frac{\chi}{E} A_i(E) B(E, T_{sun}, \Omega_{sun}) - q \exp\left(\frac{qV_i}{k_B T_{system}}\right) \int_{Eg,i}^{\infty} \frac{B\left(E, T_{system}, \pi\right)}{E} \tag{24}$$

where $A_i$ is the absorptivity of the subcell, $V_i$ is the voltage of the subcell, and $E_{g,i}$ is its bandgap. From this expression, the electric power is

$$P_{elec} = \sum_{i=1}^{2} J_{max,i} V_{max,i} \tag{25}$$

where $J_{max,i}$ and $V_{max,i}$ are the current density and voltage at the maximum power point.


### Acknowledgments

This study was supported by the UK Department for Energy Security and Net Zero (SBSP1003) and the H2020 European Research Council (Grant/Award Number: 853365). K.S. and O.M. would like to thank P. Dai and W. Xiao for support in the initial stage of the project and for fruitful discussions around the use of the genetic optimization algorithm.

### Conflicts of Interest

The authors declares no conflicts of interest

### Data Availability Statement

The data that support the findings of this study are available from the corresponding author upon reasonable request.


### References


1. E. Gibney, Could Solar Panels in Space Supply Earth with Clean Energy?, *Nature* (2023), https://doi.org/10.1038/d41586-023-00279-8.

2. M. D. Kelzenberg, P. Espinet-Gonzalez, N. Vaidya et al., "*Ultralight Energy Converter Tile for the Space Solar Power Initiative*," in IEEE 7th

World Conference on Photovoltaic Energy Conversion (WCPEC)(A Joint Conference of 45th IEEE PVSC, 28th PVSEC & 34th EU PVSEC (IEEE, Piscataway, NJ, 2018), 3357–3359, https://doi.org/10.1109/PVSC.2018.8547403.

3. E. Rodgers, J. Sotudeh, C. Mullins et al., *Space-Based Solar Power*, in AIAA 2024-4944 Session: Societal Impact of Space Activity II (Las Vegas, NV, 2024), https://doi.org/10.2514/6.2024-4944.

4. J. Mankins, N. Kaya, and M. Vasile, "*SPS-ALPHA: The First Practical Solar Power Satellite via Arbitrarily Large Phased Array (a 2011-2012 NIAC Project)*," in 10th International Energy Conversion Engineering Conference (Atlanta, GA, 2012), 3978.

5. J. -M. Choi, S.-J. Choi, and S.-H. Yi, "Case Studies on Space Solar Power in Korea,"*Space Solar Power and Wireless Transmission* 1 (2024): 27–36.

6. Y. Yang, Y. Zhang, B. Duan, D. Wang, and X. Li, "A Novel Design Project for Space Solar Power Station (SSPS-OMEGA)," *Acta Astronautica* 121 (2016): 51–58, https://doi.org/10.1016/j.actaastro.2015.12.029.

7. I. Cash, "CASSIOPeiA-A New Paradigm for Space Solar Power," *Acta Astronautica* 159 (2019): 170–178, https://doi.org/10.1016/j.actaastro.2019.03.063.

8. The Air Force Research Laboratory, *Space Power Beaming*, Retrieved April 24, 2024, https://afresearchlab.com/technology/space-power-beaming/.

9. R. Perkins, *In a First, Caltech's Space Solar Power Demonstrator Wirelessly Transmits Power in Space*, 2023. https://www.caltech.edu/about/news/in-a-first-caltechs-space-solar-power-demonstrator-wirelessly-transmits-power-in-space.

10. National Security Space Office (NSSO) Washington DC, Space-Based Solar Power As an Opportunity for Strategic Security: Phase 0 Architecture Feasibility Study, 2007. Retrieved March 26, 2025 https://apps.dtic.mil/sti/pdfs/ADA473860.pdf.

11. K. A. Horowitz, T. W. Remo, B. Smith, and A. J. Ptak, A Techno-Economic Analysis and Cost Reduction Roadmap for III-V Solar Cells (Tech. rep. National Renewable Energy Lab. (NREL), Golden, CO (United States), 2018).

12. W. N. Neil Johnson, K. Akins, J. Armstronget et al., *"Space-Based Solar Power: Possible Defense Applications and Opportunities for NRL Contributions, DTIC document, NRL/FR/7650--09-10,179*, 2009, Retrieved March 26, 2025 https://apps.dtic.mil/sti/tr/pdf/ADA513123.pdf.

13. P. Testa, M. Cagnoni, and F. Cappelluti, "*Detailed-Balance Assessment of Radiative Cooling for Multi-Junction Solar Cells under Unconcentrated and Low-Concentrated Light,"Solar Energy Materials and Solar Cells* 274 (2024):112958.

14. SpaceX, *Capabilities & Services*, Retrieved April 24, 2024 https://www.spacex.com/media/CapabilitiesServices.pdf.

15. D. Alonso-Álvarez, T. Wilson, P. Pearce, M. Führer, D. Farrell, and N. Ekins-Daukes, "Solcore: A Multi-Scale, Python-Based Library for Modelling Solar Cells and Semiconductor Materials," *Journal of Computational Electronics* 17 (2018): 1099–1123, https://doi.org/10.1007/s10825-018-1171-3.

16. L. C. Hirst, M. K. Yakes, J. H. Warner et al., "Intrinsic Radiation Tolerance of Ultra-Thin GaAs Solar Cells," *Applied Physics Letters* 109, no. 3 (2016): 033908,https://doi.org/10.1063/1.4959784.

17. A. Barthel, L. Sayre, G. Kusch, R. A. Oliver, and L. C. Hirst, "Radiation Effects in Ultra-Thin GaAs Solar Cells," *Journal of Applied Physics* 132, no. 18 (2022): 184501, https://doi.org/10.1063/5.0103381.

18. A. Barthel, S.-I. Sato, L. Sayre et al., "Open-Circuit Voltage Degradation and Trap-Assisted Tunneling in Electron and Proton-Irradiated Ultra-Thin GaAs Solar Cells," *Journal of Applied Physics* 135, no. 22 (2024): 224505, https://doi.org/10.1063/5.0205238.

19. L. Sayre, E. Camarillo Abad, P. Pearce et al., "Ultra-Thin GaAs Solar Cells with Nanophotonic Metal-Dielectric Diffraction Gratings Fabricated with Displacement Talbot Lithography," *Progress in Photovoltaics: Research and Applications* 30, no. 1 (2022): 96–108.

20. T. S. Kim, H. J. Kim, J.-H. Han, W. J. Choi, and K. J. Yu, "Flexible InGaP/GaAs Tandem Solar Cells Encapsulated with Ultrathin Thermally Grown Silicon Dioxide as a Permanent Water Barrier and an Antireflection Coating," *ACS Applied Energy Materials* 5, no. 1 (2021): 227–233.

21. T. S. Kim, H. J. Kim, D.-M. Geum, et al., "Ultra-Lightweight, Flexible InGaP/GaAs Tandem Solar Cells with a Dual-Function Encapsulation Layer," *ACS Applied Materials & Interfaces* 13, no. 11 (2021): 13248–13253, https://doi.org/10.1021/acsami.1c00006.

22. T. Takamoto, E. Ikeda, H. Kurita, M. Ohmori, M. Yamaguchi, and M.-J. Yang, "Two-Terminal Monolithic In0. 5Ga0. 5P/GaAs Tandem Solar Cells with a High Conversion Efficiency of over 30%,"*Japanese Journal of Applied Physics* 36, no. 10R (1997): 6215.

23. D. Shahrjerdi, S. W. Bedell, C. Bayram, et al., "Ultralight High-Efficiency Flexible InGaP/(In) GaAs Tandem Solar Cells on Plastic," *Advanced Energy Materials* 3, no. 5 (2013): 566–571, https://doi.org/10.1002/aenm.201200827.

24. B. Zhao, X.-S. Tang, W.-X. Huo, et al., "Characteristics of InGaP/GaAs Double Junction Thin Film Solar Cells on a Flexible Metallic Substrate," *Solar Energy* 174 (2018): 703–708, https://doi.org/10.1016/j.solener.2018.06.099.

25. M. A. Steiner, R. M. France, J. Buencuerpo, et al., "High Efficiency Inverted GaAs and GaInP/GaAs Solar Cells with Strain-Balanced GaInAs/GaAsP Quantum Wells," *Advanced Energy Materials* 11, no. 4 (2021): 2002874, https://doi.org/10.1002/aenm.202002874.

26. S. Essig, C. Allebé, T. Remo et al., "Raising the One-Sun Conversion Efficiency of III-V/Si Solar Cells to 32.8% for Two Junctions and 35.9% for Three Junctions," *Nature Energy* 2, no. 9 (2017): 1–9.

27. J. P. Samberg, C. Zachary Carlin, G. K. Bradshaw et al., "Effect of GaAs Interfacial Layer on the Performance of High Bandgap Tunnel Junctions for Multijunction Solar Cells," *Applied Physics Letters* 103, no. 10 (2013): 103503.

28. E. Barrigón, I. García, L. Barrutia, I. Rey-Stolle, and C. Algora, "Highly Conductive p++-AlGaAs/n++-GaInP Tunnel Junctions for Ultra-High Concentrator Solar Cells, *Progress in Photovoltaics: Research and Applications* 22, no. 4 (2014): 399–404.

29. Y. Gou, H. Wang, J. Wang, H. Yang, and G. Deng, "High Performance p++-AlGaAs/n++-InGaP Tunnel Junctions for Ultra-High Concentration Photovoltaics," *Optics Express* 30, no. 13 (2022): 23763–23770, https://doi.org/10.1364/OE.461302.

30. G. J. Bauhuis, P. Mulder, E. J. Haverkamp et al., "*Inverted Thin Film InGaP/GaAs Tandem Solar Cells for CPV Applications Using Epitaxial Lift Off*," in 2010 35th IEEE Photovoltaic Specialists Conference (IEEE, Piscataway, NJ, 2010), 001243–001247.

31. P. M. Pearce, E. Camarillo Abad, and L. C. Hirst, "Designing Transparent Nanophotonic Gratings for Ultra-Thin Solar Cells," *Optics Express* 30, no. 3 (2022): 4528–4542.

32. E. Camarillo Abad, H. J. Joyce, and L. C. Hirst, "Transparent Quasi-Random Structures for Multimodal Light Trapping in Ultrathin Solar Cells with Broad Engineering Tolerance," *ACS Photonics* 9, no. 8 (2022): 2724–2735.

33. N. Tavakoli, R. Spalding, A. Lambertz et al., "Over 65% Sunlight Absorption in a 1 μm Si Slab with Hyperuniform Texture," *ACS Photonics* 9, no. 4 (2022): 1206–1217.

34. J. Buencuerpo, T. E. Saenz, M. Steger, et al., "Efficient Light-Trapping in Ultrathin GaAs Solar Cells Using Quasi-Random Photonic Crystals," *Nano Energy* 96 (2022): 107080, https://doi.org/10.1016/j.nanoen.2022.107080.

35. J. J. Schermer, P. Mulder, G. J. Bauhuis, et al., "Epitaxial Lift-Off for Large Area Thin Film III/V Devices," *In: Physica Status Solidi A* 202, no. 4 (2005): 501–508, https://doi.org/10.1002/pssa.200460410.

36. M. Konagai, M. Sugimoto, and K. Takahashi, "High Efficiency GaAs Thin Film Solar Cells by Peeled Film Technology,"*Journal of Crystal Growth* 45 (1978): 277–280.

37. C.-W. Cheng, K.-T. Shiu, N. Li, S.-J. Han, L. Shi, and D. K. Sadana, "Epitaxial Lift-Off Process for Gallium Arsenide Substrate Reuse and Flexible Electronics," *Nature Communications* 4, no. 1 (2013): 1577, https://doi.org/10.1038/ncomms2583.

38. J. Schön, G. M. M. W. Bissels, P. Mulder et al., "Improvements in Ultra-Light and Flexible Epitaxial Lift-Off GaInP/GaAs/GaInAs Solar Cells for Space Applications, "*Progress in Photovoltaics: Research and Applications* 30, no. 8 (2022): 1003–1011.

39. K. L. Schulte, S. W. Johnston, A. K. Braun et al., "GaAs Solar Cells Grown on Acoustically Spalled GaAs Substrates with 27% Efficiency," *Joule* 7, no. 7 (2023): 1529–1542.

40. E. Sacchitella, S. Polly, S. Hubbard, P. Coll, and M. Bertoni, "*Demonstration of Substrate Reuse using Acoustic Spalling in GaAs based Photovoltaics*," in 2024 IEEE 52nd Photovoltaic Specialist Conference (PVSC) (IEEE, Piscataway, NJ, 2024), 1116–1119.

41. N. Vandamme, H.-L. Chen, A. Gaucher et al., "Ultrathin GaAs Solar Cells with a Silver Back Mirror," *IEEE Journal of Photovoltaics* 5, no. 2 (2014): 565–570.

42. E. C. Warmann, P. Espinet-Gonzalez, N. Vaidya, et al., "An Ultralight Concentrator Photovoltaic System for Space Solar Power Harvesting," *Acta Astronautica* 170 (2020): 443–451, https://doi.org/10.1016/j.actaastro.2019.12.032.

43. N. Vaidya, H. A. Atwater, M. D. Kelzenberg et al., "*Lightweight carbon fiber mirrors for solar concentrator applications*," in 2017 IEEE 44th Photovoltaic Specialist Conference (PVSC) (IEEE, Piscataway, NJ, 2017), 572–577.

44. N. Vaidya, and O. Solgaard, "3D Printed Optics with Nanometer Scale Surface Roughness," *Microsystems & Nanoengineering* 4, no. 1 (2018): 18.

45. K. Sun, C. A. Riedel, Y. Wang, et al., "Metasurface Optical Solar Reflectors Using AZO Transparent Conducting Oxides for Radiative Cooling of Spacecraft," *ACS Photonics* 5, no. 2 (2018): 495–501, https://doi.org/10.1021/acsphotonics.7b00991.

46. G. P. Summers, R. J. Walters, M. A. Xapsos, et al., "A New Approach to Damage Prediction for Solar Cells Exposed to Different Radiations," in*Proceedings of 1994 IEEE 1st World Conference on Photovoltaic Energy Conversion - WCPEC (A Joint Conference of PVSC, PVSEC and PSEC)*, Vol.2 (1994), 2068–2075, https://doi.org/10.1109/WCPEC.1994.521828.

47. D. Heynderickx, B. Quaghebeur, J. Wera, E. J. Daly, and H. D. R. Evans, "New Radiation Environment and Effects Models in the European Space Agency's Space Environment Information System (SPENVIS)" *Space Weather* 2, no. 10 (2004): S10S03, https://doi.org/10.1029/2004SW000073.

48. S. Sato, T. Ohshima, and M. Imaizumi, "Modeling of Degradation Behavior of InGaP/GaAs/Ge Triple-Junction Space Solar Cell Exposed to Charged Particles," *Journal of Applied Physics* 105, no. 4 (2009): 044504, https://doi.org/10.1063/1.3079522.

49. T. Takamoto, M. Kaneiwa, M. Imaizumi, and M. Yamaguchi, "InGaP/GaAs-Based Multijunction Solar Cells,"*Progress in Photovoltaics: Research and Applications* 13, no. 6 (2005): 495–511, https://doi.org/10.1002/pip.642

50. G. Yan, J.-L. Wang, J. Liu, Y.-Y. Liu, R. Wu, and R. Wang, "Electroluminescence Analysis of VOC Degradation of Individual Subcell in GaInP/GaAs/Ge Space Solar Cells Irradiated by 1.0MeV Electrons," *Journal of Luminescence* 219 (2020): 116905, https://doi.org/10.1016/j.jlumin.2019.116905.

51. M. Yamaguchi, S. J. Taylor, M.-J. Yang, S. Matsuda, O. Kawasaki, and T. Hisamatsu, "Analysis of Radiation Damage to Si Solar Cells under High-Fluence Electron Irradiation," *Japanese Journal of Applied Physics* 35, no. 7R (1996): 3918, https://doi.org/10.1143/JJAP.35.3918.

52. M. Imaizumi, S. J. Taylor, M. Yamaguchi, T. Ito, T. Hisamatsu, and S. Matsuda, "Analysis of Structure Change of Si Solar Cells Irradiated with High Fluence Electrons," *Journal of Applied Physics* 85, no. 3 (1999): 1916–1920, https://doi.org/10.1063/1.369184

53. N. J. Ekins-Daukes, H. S. Lee, T. Sasaki et al., "Carrier Removal in Lattice-Mismatched InGaP Solar Cells under 1-MeV-Electron Irradiation"*Applied Physics Letters* 85, no. 13 (2004): 2511–2513, https://doi.org/10.1063/1.1794371.

54. R. Hoheisel, M. Gonzalez, M. P. Lumb, et al., "Quantum-Well Solar Cells for Space: The Impact of Carrier Removal on End-of-Life Device Performance," *IEEE Journal of Photovoltaics* 4, no. 1 (2014): 253–259, https://doi.org/10.1109/JPHOTOV.2013.2289935.

55. S. I. Maximenko, S. R. Messenger, C. D. Cress, J. A. Freitas, and R. J. Walters, "Application of CL/EBIC-SEM Techniques for Characterization of Radiation Effects in Multijunction Solar Cells," *IEEE Transactions on Nuclear Science* 57, no. 6 (2010): 5658019, https://doi.org/10.1109/TNS.2010.2083691.

56. E. Camarillo Abad, H. J. Joyce, and L. C. Hirst, "Light Management for ever-Thinner Photovoltaics: A Tutorial Review," *APL Photonics* 9, no. 1 (2024): 011101.

57. I. Massiot, A. Cattoni, and S. Collin, "Progress and Prospects for Ultrathin Solar Cells," *Nature Energy* 5, no. 12 (2020): 959–972.

58. E. E. Perl, J. Simon, D. J. Friedman, et al., "(Al) GaInP/GaAs Tandem Solar Cells for Power Conversion at Elevated Temperature and High Concentration," *IEEE Journal of Photovoltaics* 8, no. 2 (2018): 640–645, https://doi.org/10.1109/JPHOTOV.2017.2783853.

59. Excelitas, *Space-Qualified Cover Glass*, 2025, Retrieved February 5, 2025, https://www.excelitas.com/product/space-qualified-cover-glass.

60. B. Abiri, M. Arya, F. Bohn et al., "A Lightweight Space-Based Solar Power Generation and Transmission Satellite," *arXiv Preprint arXiv: 2206.08373* (2022).

61. S.-H. Wu, G. Cossio, D. Derkacs, and E. T. Yu, "A Broadband Light-Trapping Nanostructure for InGaP/GaAs Dual-Junction Solar Cells Using Nanosphere Lithography-Assisted Chemical Etching," *Solar RRL* 8 (2024): 2400531.

62. S. P. Philipps, R. Hoheisel, T. Gandy et al., "*An Experimental and Theoretical Study on the Temperature Dependence of GaAs Solar Cells*," in 2011 37th IEEE Photovoltaic Specialists Conference (IEEE, Piscataway, NJ, 2011), 001610–001614.

63. L. M. Nieto Nieto, J. P. Ferrer Rodríguez, R. M. Campos, and P. J. Pérez Higueras, "Multi-Junction Solar Cell Measurements at Ultra-High Irradiances for Different Temperatures and Spectra,"*Solar Energy Materials and Solar Cells* 266 (2024): 112651.

64. Rocket Lab, *Z4J+ Space Solar Cell*,2024,Retrieved February 4, 2025, https://www.rocketlabusa.com/assets/Uploads/RL-SolAero-Data-Sheet-Z4J+-v8.pdf.

65. G. A. Landis,"Space Photovoltaics for Extreme High-Temperature Missions,"Photovoltaics for Space (Elsevier, 2023), 393–410.

66. G. A. Landis, D. Merritt, R. P. Raffaelle, and D. Scheiman, "*High-Temperature Solar Cell Development*," in 18th Space Photovoltaic Research and Technology Conference (Cleveland, OH, 2005).

67. J. F. Ziegler and J. P. Biersack,"The Stopping and Range of Ions in Matter," in Treatise on Heavy-Ion Science, ed D. A. Bromley (Springer, Boston, MA, 1985).

68. D. Drouin, A. R. Couture, D. Joly, X. Tastet, V. Aimez, and R. Gauvin, "CASINO V2. 42—a Fast and Easy-to-use Modeling Tool for Scanning

Electron Microscopy and Microanalysis Users," *Scanning* 29, no. 3 (2007): 92–101.

69. G. P. Summers, E. A. Burke, and M. A. Xapsos, "*Displacement Damage Analogs to Ionizing Radiation Effects". in: Radiation Measurements*24, no. 1 (1995): 1–8, https://doi.org/10.1016/1350-4487(94)00093-G issn: 13504487.

70. I. Jun, M. A. Xapsos, S. R. Messenger, et al., "Proton Nonionizing Energy Loss (NIEL) for Device Applications," *IEEE Transactions on Nuclear Science* 50, no. 6 (2003): 1924–1928, https://doi.org/10.1109/TNS.2003.820760.

71. M. Sotoodeh, A. H. Khalid, and A. A. Rezazadeh, "Empirical Low-Field Mobility Model for III-V Compounds Applicable in Device Simulation Codes," *Journal of Applied Physics* 87, no. 6 (2000): 2890–2900, https://doi.org/10.1063/1.372274.

72. M. Yamaguchi, C. Uemura, A. Yamamoto, and A. Shibukawa, "Electron Irradiation Damage in Radiation-Resistant InP Solar Cells," *Japanese Journal of Applied Physics* 23, no. 3R (1984): 302–307, https://doi.org/10.1143/JJAP.23.302.

73. F. Lei, R. R. Truscott, C. S. Dyer, et al., "MULASSIS: A Geant4-Based Multilayered Shielding Simulation Tool," *IEEE Transactions on Nuclear Science* 49, no. 6 (2002): 2788–2793, https://doi.org/10.1109/TNS.2002.805351.

74. G. P. Ginet, T. P. O'Brien, S. L. Huston, et al., "AE9, AP9 and SPM: New Models for Specifying the Trapped Energetic Particle and Space Plasma Environment," *Space Science Reviews* 179, no. 1–4 (2013): 579–615, https://doi.org/10.1007/s11214-013-9964-y.

75. M. Buehren, *Differential Evolution*, MATLAB Central File Exchange, Retrieved December 6, 2023, https://www.mathworks.com/matlabcentral/fileexchange/18593-differential-evolution.

76. K. C. Johnson, *Grating Diffraction Calculator (GD-Calc)*, Accessed 06 July 2022, https://codeocean.com/capsule/8614002/tree/v3.

77. F.-A. Fortin et al., "DEAP: Evolutionary Algorithms Made Easy," *The Journal of Machine Learning Research* 13, no. 1 (2012): 2171–2175.

78. W. Xiao, P. Dai, H. Johnson Singh et al., "Flexible Thin Film Optical Solar Reflectors with Ta2O5-Based Multimaterial Coatings for Space Radiative Cooling," *APL Photonics* 8, no. 9 (2023): 090802.

**Supporting Information**

Additional supporting information can be found online in the Supporting Information section.